

Three Dimensional Distorted Black Holes

Steven Brandt⁽¹⁾, Karen Camarda^(2,3), Edward Seidel^(4,5,6), and Ryoji Takahashi^(4,7)

⁽¹⁾190 Drexel Ave., Lansdowne, PA 19050

⁽²⁾Department of Chemical and Petroleum Engineering, University of Kansas,
Lawrence, KS 66045

⁽³⁾Department of Physics and Astronomy, Washburn University, Topeka, KS 66621

⁽⁴⁾Max-Planck-Institut für Gravitationsphysik, Am Muehlenberg 5, D-14476 Golm, Germany

⁽⁵⁾National Center for Supercomputing Applications, Beckman Institute, 405 N. Mathews Ave.,
Urbana, IL 61801

⁽⁶⁾Departments of Astronomy and Physics, University of Illinois, Urbana, IL 61801

⁽⁷⁾Theoretical Astrophysics Center, Juliane Maries Vej 30, 2100 Copenhagen, Denmark

(November 30, 2018)

Abstract

We present three-dimensional, *non-axisymmetric* distorted black hole initial data which generalizes the axisymmetric, distorted, non-rotating [1] and rotating [2] single black hole data developed by Bernstein, Brandt, and Seidel. These initial data should be useful for studying the dynamics of fully 3D, distorted black holes, such as those created by the spiraling coalescence of two black holes. We describe the mathematical construction of several families of such data sets, and show how to construct numerical solutions. We survey quantities associated with the numerically constructed solutions, such as ADM masses, apparent horizons, measurements of the horizon distortion, and the maximum possible radiation loss (*MRL*).

04.25.Dm, 04.30.Db, 97.60.Lf, 95.30.Sf

arXiv:gr-qc/0206070v2 12 Nov 2002

I. INTRODUCTION

Black hole studies have received significant attention in numerical relativity over the past several years, as the computers needed to solve the Einstein equations grow in power. The need for computer generated templates of gravitational waves has become more pressing since gravitational wave detectors, such as LIGO and GEO600, are nearing completion and should begin taking data in about a year [3,4]. Binary black hole coalescence events are considered to be prime candidates for the first detection of gravitational waves [5].

Several theoretical approaches have been developed for treating these systems. So far, the post-Newtonian approximation (PN) has provided a good understanding of the early slow adiabatic inspiral, or “far-limit”, phase of these systems [6,7,8,9,10]. Similarly, for the final moments, when the black holes are close enough to each other to sit inside a common gravitational well, one can successfully apply the “close limit” approximation (CL) [11], which effectively describes the whole system as a perturbation of a single black hole which rapidly “rings-down” to stationarity. Before this last stage, though, when the black holes are still close to the *innermost stable circular orbit*, the orbital dynamics are expected to yield to a plunge and coalescence. No approximation method can be applied in this highly nonlinear phase and it is generally expected that one can only treat the system by a full numerical integration of Einstein’s equations.

Ideally, one would like to start a full nonlinear integration of the Einstein equations with initial data that correspond to black holes in the early adiabatic inspiral phase. Such data would be straight-forward to compute [12], and would correspond well to a realizable astrophysical situation. Unfortunately, there are several technical difficulties involved in numerically evolving such a system all the way through coalescence to ringdown. Accordingly, in order to develop and test fully nonlinear numerical codes while the difficulties are being resolved, the strategy has been to evolve initial data that can be used as a model of the merger event. For example, initial data corresponding to holes which are initially very close together have been evolved [13,14,15], as have data sets which correspond to a single very distorted hole [16,17,18].

In this paper we describe initial data sets which correspond to three-dimensional distorted black holes, both with rotation and without. The formalism employed extends the axisymmetric work done by Bernstein, Brandt, and Seidel [1,2]. Although these data sets and their evolution have already been described briefly in several places [18,19,20,21,22,23,24], in this paper, we provide a more complete description of them.

The paper is organized as follows. In Section II we describe the mathematical setup and numerical construction of the data sets. In Section III we give results of parameter studies of their properties, such as ADM masses, apparent horizon positions, distortion measures, and maximal radiation loss. Then, we conclude our results in Section IV.

II. CONSTRUCTING DISTORTED 3D BLACK HOLES

The standard approach to constructing initial data for Einstein’s equations is to consider a 3+1 split (3 space and 1 time) of the full four-dimensional theory. In this way the equations divide naturally into two classes: four constraint equations, and six evolution equations. The procedure for performing the split is described extensively in many places, notably in the

review article by York [25]. The constraints, which are elliptic in nature, relate the 3-metric γ_{ij} and extrinsic curvature K_{ij} at any coordinate time t . In our case, we solve the constraints to obtain data sets for some initial time labeled by $t = 0$. The constraints can be further split into the Hamiltonian constraint and the momentum constraints. Here, we consider vacuum spacetimes, for which the Hamiltonian constraint is

$$R + (\text{tr}K)^2 - K^{ij}K_{ij} = 0, \quad (1)$$

and the three momentum constraints are

$$D_i(K^{ij} - \gamma^{ij}\text{tr}K) = 0, \quad (2)$$

where R and D_i are the scalar curvature and covariant derivative associated with the 3-metric γ_{ij} .

To solve the constraints, it is common to use York's conformal decomposition method [25]. This method starts by factoring out a function ψ , known as the conformal factor, from the 3-metric and extrinsic curvature tensor components in the following way:

$$\gamma_{ij} = \psi^4 \hat{\gamma}_{ij}, \quad (3)$$

$$K_{ij} = \psi^{-2} \hat{K}_{ij}. \quad (4)$$

If we use this decomposition, and restrict ourselves to initial slices with vanishing $\text{tr}K = \gamma^{ij}K_{ij}$, the constraint equations take the following form:

$$\hat{\Delta}\psi = \frac{1}{8}\psi\hat{R} - \frac{1}{8}\psi^{-7}\hat{K}^{ij}\hat{K}_{ij} \quad (5)$$

$$\hat{D}_i\hat{K}^{ij} = \partial_i\hat{K}^{ij} + \hat{\Gamma}_{ik}^i\hat{K}^{kj} + \hat{\Gamma}_{ik}^j\hat{K}^{ik} = 0, \quad (6)$$

where $\hat{\Delta}$ is the Laplacian, \hat{R} the scalar curvature, and $\hat{\Gamma}_{ik}^j$ the Christoffel symbol associated with the conformal 3-metric $\hat{\gamma}_{ij}$. Note that the conformal factor does not appear in the momentum constraint equations. This allows us to use the following procedure to derive initial data. First, one specifies the conformal 3-metric $\hat{\gamma}_{ij}$ freely. Then, the momentum constraint equations are solved for the conformal extrinsic curvature. Finally, one solves the Hamiltonian constraint for the conformal factor. This is the procedure we use to create the 3D black hole initial data sets described below.

A. Distorted non-rotating black hole

As part of his thesis work, Bernstein studied initial data sets corresponding to single black holes which were non-rotating, distorted, and axisymmetric [1]. For these non-rotating black holes, the extrinsic curvature was taken to vanish. In this case, the vacuum momentum constraint equations are satisfied identically, and the Hamiltonian constraint reduces to

$$\hat{\Delta}\psi = \frac{1}{8}\psi\hat{R}. \quad (7)$$

The form of the conformal 3-metric was that used by Brill in his study of pure gravitational wave spacetimes [26]. Using spherical-polar coordinates, one can write the 3-metric as

$$dl^2 = \psi^4 [e^{2q}(dr^2 + r^2 d\theta^2) + r^2 \sin^2 \theta d\phi^2], \quad (8)$$

where q is the Brill “packet” which takes some functional form. Using this ansatz with (7) leads to an elliptic equation for ψ which must be solved numerically. The inner boundary of our computational domain is the throat of the black hole, and there we apply an isometry condition on ψ which maps the region exterior to the throat to another asymptotically flat region interior to it. At the outer boundary, we apply the Robin condition which requires $\psi \sim O(r^{-1})$ as $r \rightarrow \infty$ is used as the outer boundary condition. The choice of $q = 0$ produces the spherically symmetric Schwarzschild solution in isotropic coordinates. In Bernstein’s work, a logarithmic radial coordinate η is used, related to the isotropic radial coordinate r by

$$\eta = \ln\left(\frac{2r}{M_0}\right), \quad (9)$$

where M_0 is the mass of the Schwarzschild black hole that results from setting $q = 0$. In this coordinate system, the 3-metric is

$$dl^2 = \tilde{\psi}^4 [e^{2q}(d\eta^2 + d\theta^2) + \sin^2 \theta d\phi^2], \quad (10)$$

and the Schwarzschild solution is

$$\tilde{\psi} = \sqrt{2M_0} \cosh\left(\frac{\eta}{2}\right). \quad (11)$$

Note that the conformal factor in the η -coordinate system, $\tilde{\psi}$, differs from that in the isotropic radial coordinate system by a factor of $r^{1/2}$.

The Hamiltonian constraint in this coordinate system is

$$\frac{\partial^2 \tilde{\psi}}{\partial \eta^2} + \frac{\partial^2 \tilde{\psi}}{\partial \theta^2} + \cot \theta \frac{\partial \tilde{\psi}}{\partial \theta} = -\frac{1}{4} \tilde{\psi} \left(\frac{\partial^2 q}{\partial \eta^2} + \frac{\partial^2 q}{\partial \theta^2} - 1 \right). \quad (12)$$

The throat of the black hole is located at $r = M_0/2$, or $\eta = 0$. The isometry condition across the throat in the η coordinate system takes the particular simple form $\gamma_{ij}(\eta) = \pm \gamma_{ij}(-\eta)$, which for the conformal factor becomes $\tilde{\psi}(\eta) = \tilde{\psi}(-\eta)$. At the outer boundary we require that $\tilde{\psi}$ have the same behavior as the spherically symmetric solution.

The Brill wave function q was chosen to have the following form, which obeys the boundary conditions but is otherwise arbitrary. Specifically Brill showed that in order for the mass of the hypersurface to be well defined, q must vanish on the axis and decrease radially at least as fast as $e^{-2\eta}$. In this paper, we choose q to be of the form used by Bernstein:

$$q(\eta, \theta) = Q_0 \sin^n \theta \left[e^{-\left(\frac{\eta+\eta_0}{\sigma}\right)^2} + e^{-\left(\frac{\eta-\eta_0}{\sigma}\right)^2} \right]. \quad (13)$$

Roughly speaking, Q_0 is the amplitude of Brill wave, η_0 its radial location, and σ its width. Regularity along the axis requires that the exponent n must be even. We characterize initial data sets by the parameters (Q_0, η_0, σ, n) .

Note that an even exponent n results in data that have equatorial plane symmetry, so that only θ in the range $0 \leq \theta \leq \pi/2$ (or equivalently, $\pi/2 \leq \theta \leq \pi$) need to be considered.

We chose to extend Bernstein's work to 3D by multiplying the Brill wave function q by a factor which has azimuthal dependence. The particular form of this factor was $1 + c \cos^2 \phi$, giving the q -function

$$q(\eta, \theta, \phi) = Q_0 \sin^n \theta \left[e^{-\left(\frac{\eta+\eta_0}{\sigma}\right)^2} + e^{-\left(\frac{\eta-\eta_0}{\sigma}\right)^2} \right] (1 + c \cos^2 \phi). \quad (14)$$

Here, one can see that the above axisymmetric case is recovered by setting $c = 0$. Now the Hamiltonian constraint takes on the more complicated form

$$\begin{aligned} & \frac{\partial^2 \tilde{\psi}}{\partial \eta^2} + \frac{\partial^2 \tilde{\psi}}{\partial \theta^2} + \cot \theta \frac{\partial \tilde{\psi}}{\partial \theta} + \csc^2 \theta e^{2q} \frac{\partial^2 \tilde{\psi}}{\partial \phi^2} + 2 \csc^2 \theta e^{2q} \frac{\partial q}{\partial \phi} \frac{\partial \tilde{\psi}}{\partial \phi} = \\ & -\frac{1}{4} \tilde{\psi} \left[\frac{\partial^2 q}{\partial \eta^2} + \frac{\partial^2 q}{\partial \theta^2} + 2e^{2q} \csc^2 \theta \frac{\partial^2 q}{\partial \phi^2} + 3e^{2q} \csc^2 \theta \left(\frac{\partial q}{\partial \phi} \right)^2 - 1 \right]. \end{aligned} \quad (15)$$

In this case, we characterize our initial data sets by the parameters $(Q_0, \eta_0, \sigma, c, n)$.

Notice that we still have equatorial plane symmetry with this q . We also have sufficient symmetry in the azimuthal angle ϕ to restrict ourselves to the range $0 \leq \phi \leq \pi/2$. This allows us to perform computations in only one octant, resulting in a great savings in computational time. However, for consistency with the non-axisymmetric rotating cases in which one cannot apply any symmetries, we solve it on a full grid domain. Note also that although setting $n = 2$ is valid in axisymmetry, when $c \neq 0$, n must be at least 4 for the right hand side of (15) to be regular. Using the same boundary conditions as above, we can solve (15) for the conformal factor $\tilde{\psi}$ numerically on this spherical grid.

In order to evolve these initial data, we interpolate the conformal factor $\tilde{\psi}$ and its derivatives onto a Cartesian grid. As a test of our initial data solver, we compute the residual of the Hamiltonian constraint, H , on this Cartesian grid at various resolutions. We expect to see second order convergence in the grid spacing.

Fig. 1 shows the logarithm of the residual of the Hamiltonian constraint, H , on the x -axis at three different resolutions for the data set $(Q_0, \eta_0, \sigma, c, n) = (-0.5, 0, 1, 1, 4)$. The values of H are rescaled so that they would coincide for perfect second order convergence. We obtain near second order convergence, although some error is seen for the coarsest resolution.

This family of initial data sets of isometric embedding [27], and their evolution as perturbations of the Schwarzschild black hole [20,21] have been studied. In Section III, we study various physical properties of these black holes as a function of the parameters of this initial data.

B. Distorted rotating black hole

Brandt and Seidel extended the above non-rotating axisymmetric initial data sets of Bernstein to include rotation [2,17,28]. In the same way that Bernstein's data sets correspond to a Schwarzschild black hole surrounded by a gravitational wave, their data sets correspond to either a Kerr or Bowen and York black hole surrounded by a gravitational wave. For the rotating case, the 3-metric takes the form

$$dl^2 = \tilde{\psi}^4 \left[e^{2(q-q_0)} (d\eta^2 + d\theta^2) + \sin^2 \theta d\phi^2 \right]. \quad (16)$$

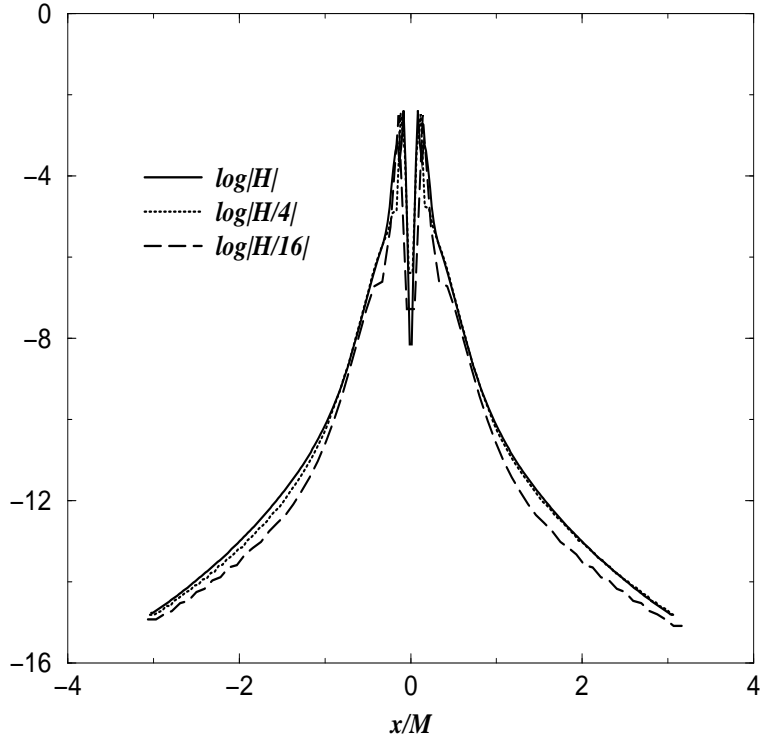


FIG. 1. We show the convergence of the residual of the Hamiltonian constraint for distorted non-rotating black hole initial data with parameter set $(Q_0, \eta_0, \sigma, c, n) = (-0.5, 0, 1, 1, 4)$. H is plotted for Cartesian grid sizes (resolutions) $259^3(0.024M)$, $131^3(0.047M)$, and $67^3(0.095M)$. As indicated, values computed at lower resolutions are rescaled such that they would coincide for perfect second order convergence.

Note that a function q_0 has been subtracted from the Brill wave function q . The form of q_0 is found by setting the 3-metric equal to the spatial part of the Kerr metric and setting $q = 0$. Apart from the function q_0 this is the same three-metric used for the non-rotating, distorted black hole spacetime. Here the logarithmic coordinate η is related to the Boyer-Lindquist coordinate r by

$$r = r_+ \cosh^2(\eta/2) - r_- \sinh^2(\eta/2), \quad (17)$$

where $r_{\pm} = M \pm \sqrt{M^2 - a^2}$. When considered together with the extrinsic curvature, this 3-metric allows for a distinct class of initial data: distorted Kerr or Bowen and York black holes. To obtain initial data for a distorted Kerr black hole, one can set the conformal extrinsic curvature tensor \hat{K}_{ij} to that which would be obtained for the standard Kerr metric, as shown in [2].

In order to obtain a distorted Bowen and York black hole, one can use the Bowen and York expression for the conformal extrinsic curvature [29]:

$$\hat{K}_{ij} = \begin{pmatrix} 0 & 0 & 3J \sin^2 \theta \\ 0 & 0 & 0 \\ 3J \sin^2 \theta & 0 & 0 \end{pmatrix}, \quad (18)$$

where J is the total angular momentum of spacetime¹. The conformal metric used in this case is that resulting from setting $q_0 = 0$ in (16) which is related to the conformally flat metric.

It is not possible to extend the axisymmetric distorted Bowen and York black holes to 3D in the same way as in the non-rotating case. This is because if one allows the Brill wave function q to depend on the azimuthal angle ϕ , it can be shown that the η -component of the momentum constraint equation reduces to $J\partial_\phi q = 0$; i.e. for the Bowen and York form of the conformal extrinsic curvature, one cannot have both angular momentum and a Brill wave function with azimuthal dependence. Instead, to extend the rotating case to 3D, we use the conformally flat metric that results from setting $q = q_0$ in equation (16), and place the ϕ -dependence in the conformal extrinsic curvature. The general form of \hat{K}_{ij} ² used is

$$\hat{K}_{ij} = m \sin(m\phi) \begin{pmatrix} h_0 & h_1 & 0 \\ h_1 & h_x - h_0 & 0 \\ 0 & 0 & -h_x \sin^2 \theta \end{pmatrix} + \begin{pmatrix} 0 & 0 & \hat{K}_{\eta\phi} \\ 0 & 0 & \hat{K}_{\theta\phi} \\ \hat{K}_{\eta\phi} & \hat{K}_{\theta\phi} & 0 \end{pmatrix}, \quad (19)$$

where

$$\hat{K}_{\eta\phi} = \sin^2 \theta [3J + \cos(m\phi) \frac{1}{\sin^3 \theta} \partial_\theta (\sin^4 \theta g)], \quad (20)$$

$$\hat{K}_{\theta\phi} = \cos(m\phi) \sin \theta (m^2 v - \sin^2 \theta \partial_\eta g). \quad (21)$$

Note that we have made all ϕ -dependence in the problem explicit. The functions v, g, h_0, h_x , and h_1 that appear above depend only η and θ . Below we outline a procedure for finding forms for these functions that result in a conformal extrinsic curvature that satisfies the momentum constraint. The quantity J is a constant.

We choose the functions h_0 and h_1 to have the form

$$h_0 = \partial_\eta \Omega - \frac{1}{\sin \theta} \partial_\theta (\sin \theta \Lambda), \quad (22)$$

$$h_1 = \partial_\eta \Lambda + \frac{1}{\sin \theta} \partial_\theta (\sin \theta \Omega). \quad (23)$$

¹ J is both a free parameter and the total angular momentum (ADM angular momentum) of the initial data, and hence of the space time. This is always true. It does not matter whether the data is axisymmetric or not, because the total angular momentum is defined at infinity (i.e. it is not local). Notice that when there are symmetries, it is possible to define not only the angular momentum at infinity, but also a quasi-local angular momentum by integrating the Killing vector (and both coincide). However, even this quasi-local definition is possible for our case: for the non-axisymmetric extrinsic curvature described in this section, since our data is conformally flat and a maximal slice, one can use the conformal Killing vector to define this quasi-local angular momentum as described in Ref. [30]

²There is a way to construct “all” the solutions in an explicit form: namely construct all the solutions in terms of derivatives of two free functions as in Theorem 14 [31]

If $m = 0$, the momentum constraint equations are satisfied trivially. If $m \neq 0$, the η , θ , and ϕ component of momentum constraints become, respectively,

$$(\partial_\eta^2 - 1 + \partial_\theta^2 + 2 \cot \theta \partial_\theta) \Omega = (4 \cos \theta + \sin \theta \partial_\theta) g, \quad (24)$$

$$(\partial_\eta^2 - 1 + \partial_\theta^2 + 2 \cot \theta \partial_\theta) \Lambda = -\csc \theta m^2 v - \partial_\theta h_x - 2 \cot \theta h_x + \sin \theta \partial_\eta g, \quad (25)$$

$$h_x + 2 \cos \theta v + \sin \theta \partial_\theta v = 0. \quad (26)$$

Now we expand all functions in trigonometric functions of θ to the lowest order at which everything can be solved. After some calculations, we found the minimum collection of terms for g and Ω to be

$$g = (\tilde{g}_0 + \tilde{g}_2 \sin^2 \theta) \cos \theta \quad (27)$$

$$\Omega = \sin^2 \theta \tilde{\Omega}_2 + \sin^4 \theta \tilde{\Omega}_4 \quad (28)$$

Note that for this discussion, tildes are used to indicate functions which depend on η alone.

One substitutes these equations into the η -component of the momentum constraint (24). By doing this, one obtains an equation which can be written

$$0 = \tilde{E}_0 + \tilde{E}_2 \cos(2\theta) + \tilde{E}_4 \cos(4\theta). \quad (29)$$

Obviously, each coefficient function \tilde{E}_i must vanish. Setting \tilde{E}_4 to zero gives

$$\tilde{g}_2 = \frac{1}{7}(25\tilde{\Omega}_4 - \partial_\eta^2 \tilde{\Omega}_4). \quad (30)$$

Setting $\tilde{E}_0 + \tilde{E}_2 = 0$ gives

$$\tilde{g}_0 = \frac{3}{2}\tilde{\Omega}_2. \quad (31)$$

Next, we introduce an arbitrary function \tilde{y} , and redefine $\tilde{\Omega}_2$ to be

$$\tilde{\Omega}_2 = \tilde{y} - \frac{6}{7}\tilde{\Omega}_4. \quad (32)$$

Using the relation $\tilde{E}_2 - \tilde{E}_0 = 0$ we obtain

$$\tilde{\Omega}_4 = \frac{7}{2}(2\partial_\eta^2 \tilde{y} - 3\tilde{y}). \quad (33)$$

At this point, we have used the η -component of the momentum constraint (24) to define the functions Ω and g in terms of the arbitrary function $\tilde{y}(\eta)$.

In order to solve the θ -component of the momentum constraint (25), we expand the functions Λ and v as follows:

$$\Lambda = \sin(2\theta) \tilde{\Lambda}_2 + \sin(4\theta) \tilde{\Lambda}_4, \quad (34)$$

$$v = \tilde{v} [\cos \theta - \cos(3\theta)]. \quad (35)$$

Plugging these expansions into the θ -component of the momentum constraint, and using the ϕ -component of the momentum constraint to write h_x in terms of v , results in an equation which can be written

$$0 = \tilde{L}_1 \cos \theta + \tilde{L}_3 \cos (3\theta) + \tilde{L}_5 \cos (5\theta). \quad (36)$$

Clearly, it must be the case that $\tilde{L}_1 = \tilde{L}_3 = \tilde{L}_5 = 0$. Setting $\tilde{L}_1 + \tilde{L}_3 + \tilde{L}_5 = 0$ gives

$$\tilde{\Lambda}_2 = -2\tilde{\Lambda}_4. \quad (37)$$

In order to solve for $\tilde{\Lambda}_4$, we set $\tilde{L}_1/32 + \tilde{L}_3/48 = 0$, which eliminates the derivatives of $\tilde{\Lambda}_4$. This gives

$$\tilde{\Lambda}_4 = \frac{4(m^4 - 16)\tilde{v} + 15\partial_\eta\tilde{y} - 9\partial_\eta^3\tilde{y}}{96}. \quad (38)$$

The next step is to define \tilde{v} and \tilde{y} in terms of an arbitrary function \tilde{x} :

$$\tilde{v} = \sum_{n=1,3,5} a_n \partial_\eta^n \tilde{x}, \quad (39)$$

$$\tilde{y} = \tilde{x} + a_7 \partial_\eta^2 \tilde{x}. \quad (40)$$

Finally, setting $\tilde{L}_5 = 0$ and using the above substitutions produces an equation which can be written

$$A_1 \partial_\eta \tilde{x} + A_3 \partial_\eta^3 \tilde{x} + A_5 \partial_\eta^5 \tilde{x} + A_7 \partial_\eta^7 \tilde{x} = 0 \quad (41)$$

Solving the linear system that results from setting each A_i to zero gives

$$a_1 = \frac{-15}{32 - 20m^2}, \quad (42)$$

$$a_3 = \frac{39}{80 - 50m^2}, \quad (43)$$

$$a_5 = \frac{3}{20(-8 + 5m^2)}, \quad (44)$$

$$a_7 = \frac{16 - m^2}{-40 + 25m^2}. \quad (45)$$

We now have analytic forms for the equations v , g , h_0 , h_1 , and h_x which are functions of an arbitrary function $\tilde{x}(\eta)$ and which satisfy the momentum constraint equations. In this work, we choose the function \tilde{x} to be the Brill wave function without the $\sin^n \theta$ factor:

$$\tilde{x} = Q_0 [e^{-(\frac{\eta-\eta_0}{\sigma})^2} + e^{-(\frac{\eta+\eta_0}{\sigma})^2}]. \quad (46)$$

Note that if we set the parameter m to zero, the problem reduces to an axisymmetric problem, although not to the one studied by Brandt and Seidel. If we further set $Q_0 = 0$, we recover the Bowen and York solution.

Using the conformal extrinsic curvature derived above, we can solve the Hamiltonian constraint numerically for the conformal factor $\tilde{\psi}$:

$$\frac{\partial^2 \tilde{\psi}}{\partial \eta^2} + \frac{\partial^2 \tilde{\psi}}{\partial \theta^2} + \cot \theta \frac{\partial \tilde{\psi}}{\partial \theta} + \csc^2 \theta \frac{\partial^2 \tilde{\psi}}{\partial \phi^2} = \frac{1}{4} \tilde{\psi} - \frac{1}{8} \hat{K}_{ij} \hat{K}^{ij} \tilde{\psi}^{-7} \quad (47)$$

We then interpolate these data onto a 3D Cartesian grid.

Fig. 2 shows the logarithm of the residual of the Hamiltonian constraint, H , on the x -axis at three different resolutions for the data set $(Q_0, \eta_0, \sigma, J, m) = (1, 0, 1, 35, 2)$. The values of H are rescaled so that they would coincide for perfect second order convergence. As in the non-rotating case, we see near second order convergence, especially for the higher two resolutions.

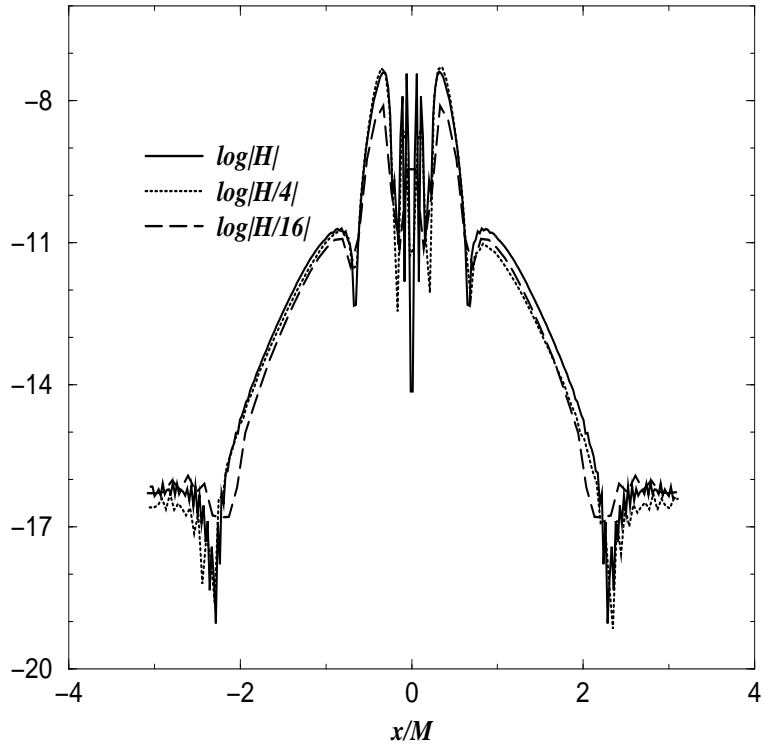


FIG. 2. We show the convergence of the residual of the Hamiltonian constraint for distorted, rotating black hole initial data with the parameter set $Q_0 = 1.0, \eta_0 = 0, \sigma = 1, J = 35.0$, and $m = 2$. H is plotted for Cartesian grid sizes (resolutions) $259^3(0.024M)$, $131^3(0.047M)$, and $67^3(0.095M)$. As indicated, values computed at lower resolutions are rescaled so that they would coincide for perfect second order convergence.

III. A SURVEY OF DISTORTED BLACK HOLE INITIAL DATA SETS

In this Section we do a parameter study of the above initial data. For all cases considered, we choose the wave location and width parameters η_0 and σ to be 0 and 1, respectively. This corresponds to a Brill wave located on the throat with unit width. This choice is made because we are concerned about the necessary closeness of the outer computational boundary for the future nonlinear evolutions of these data sets.

A. Analysis of the ADM mass

Although one cannot define a local energy density of the gravitational field in general relativity, if the spacetime is asymptotically flat, one can define the energy of an isolated source as measured by a distant observer. Arnowitt, Deser, and Misner defined an energy in natural way for their 3+1 formalism [32]. Ó Murchandha and York modified their expression to use the variables in York's conformal decomposition method [33]. For conformal metrics which fall off fast enough with radius, their expression for the ADM mass is

$$M = -\frac{1}{2\pi} \oint_{\infty} D_i \psi dS^i. \quad (48)$$

Since our numerical domains have finite extent, we perform this integral over a sphere of large constant radius R , resulting in the following expression:

$$M = -\frac{R^2}{2\pi} \int_0^{2\pi} d\phi \int_0^\pi \frac{\partial \psi}{\partial r} \sin \theta d\theta. \quad (49)$$

In the η -coordinate system, this equation is

$$M = -\frac{1}{2\pi} \sqrt{\frac{M_0}{2} \eta_{max}} \int_0^\pi d\phi \int_0^\pi \left(\frac{\partial \tilde{\psi}}{\partial \eta} - \frac{\tilde{\psi}}{2} \right) \Big|_{\eta_{max}} \sin \theta d\theta. \quad (50)$$

When we state the ADM mass for a spacetime, we have confirmed that the error involved in computing the integral at a finite radius is not significant by making sure that the integral as a function of R is approaching a constant value where we are performing the integration.

For distorted non-rotating cases, we studied a variety of Brill wave amplitudes (Q_0) and azimuthal factors (c). To better understand the results, we first note that the azimuthal factor in the Brill wave function can be written

$$1 + c \cos^2 \phi = 1 + \frac{c}{2} + \frac{c}{2} \cos(2\phi). \quad (51)$$

That is, it has a constant part and an oscillatory part. The constant part by itself in effect increases the Brill wave amplitude.

Fig. 3 shows plots of ADM masses as functions of Q_0 and c . In panel 1 (for $c = -2$), the constant term in the azimuthal factor vanishes. One expects that for this case, one will obtain the same spacetime if one changes the sign of the Brill wave amplitude, only rotated. Thus, the ADM mass should be symmetric about $Q_0 = 0$, which is seen. In panel 2 (for $c = -1$), we see the results consistent with an effective amplitude decrease. For $Q_0 < 0$,

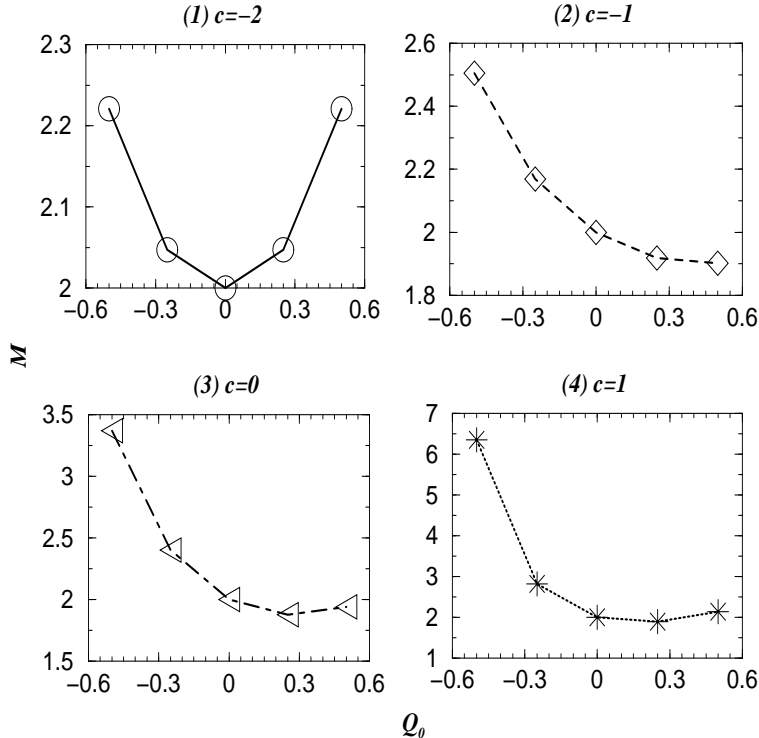


FIG. 3. We show the ADM mass as a function of the Brill wave parameters Q_0 for four different values of c . The wave location and width parameters η_0 and σ are 0 and 1, respectively. Grid size (resolution) is 131^3 ($\Delta x = 0.2$).

the mass increases with decreasing Q_0 , and has lower values than the corresponding Q_0 in axisymmetry. For $Q_0 > 0$, the minimum in the mass occurs at a higher value of Q_0 than the axisymmetric case, and it has a lower value at any given c . In panel 3 ($c = 0$), the results are what one might expect given Bernstein's results in axisymmetry, and the form of the azimuthal factor in the q -function. Bernstein found that in axisymmetry, when one increases Q_0 , the ADM mass initially decreases, then increases with Q_0 . Although the initial increase seems counter-intuitive, he points out that when one increases the amplitude of the Brill wave, it is possible to simultaneously decrease the mass of the underlying black hole, which can give a net decrease in the mass. Bernstein also found that for the negative Brill wave amplitudes, the ADM mass increases monotonically with decreasing Q_0 . Our results for $c = 0$ agree with the above Bernstein's results. Panel 4 ($c = 1$) shows the same features as the panel 3. However, the minimum in the ADM occurs at a lower value of Q_0 and is larger at $Q_0 = 0.6$. From Eq. (14), the case of $Q_0 = 0$ corresponds to a Schwarzschild black hole. For this case, the ADM mass should be the Schwarzschild mass M_0 , which in this work is chosen to be 2. This is the value seen.

The effect of the oscillatory part of the azimuthal factor by itself can be seen in panel 1 of Fig. 3. Increasing the absolute value of c increases the ADM mass. For positive values c , both the constant term and the oscillatory term are increased, and the effect of the ADM mass has the same character as increasing the Brill wave amplitude. For negative values of c , the situation is more complicated. For the range $-2 \leq c \leq 0$, the magnitude of the constant term decreases with decreasing c while the magnitude of the oscillatory term increase. The

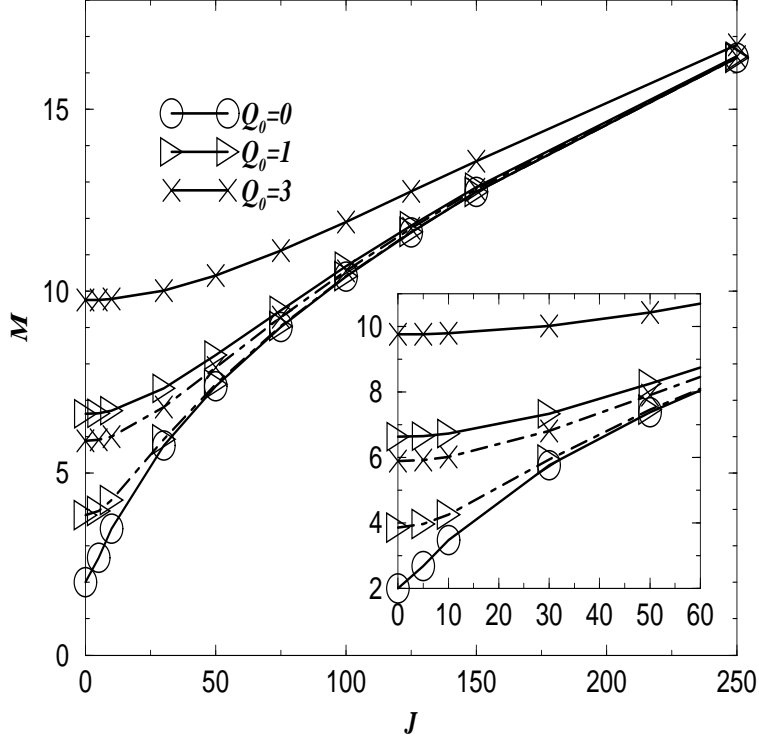


FIG. 4. We show the ADM mass M as a function of the total angular momentum J for various values of the Brill wave amplitude Q_0 . The solid lines show the axisymmetric cases ($m = 0$), and the dashed line shows the non-axisymmetric cases ($m = 2$).

relative effect on the ADM mass within this range depends on the sign of the Brill wave amplitude.

For distorted rotating cases, we investigate how the ADM mass behaves as a function of the Brill wave amplitude (Q_0), the total angular momentum (J), and the azimuthal dependence variable (m).

Fig. 4 shows the ADM mass M as a function of the total angular momentum J for various values of the Brill wave amplitude Q_0 . The ADM masses increase monotonically with increasing amplitude for both axisymmetric and non-axisymmetric cases. When the total angular momentum J is small, it is not effective for increasing the ADM mass.

We also observe the different results when comparing axisymmetric and non-axisymmetric cases. In the axisymmetric cases ($m = 0$), the non-vanishing components of the conformal extrinsic curvature are $\hat{K}_{\eta\phi}$ (20) and $\hat{K}_{\theta\phi}$ (21). By substituting Eq. (46) into Eqs. (20), we see that the component $\hat{K}_{\eta\phi}$ can be written

$$\hat{K}_{\eta\phi}(m = 0) = f_0 + f_2 \cos(2\theta) + f_4 \cos(4\theta) + f_6 \cos(6\theta) \quad (52)$$

where

$$f_0 = \frac{3}{2}J + \frac{1}{8}\tilde{g}_0 + \frac{1}{16}\tilde{g}_2 \quad (53)$$

$$f_2 = -\frac{3}{2}J + \frac{1}{2}\tilde{g}_0 + \frac{5}{16}\tilde{g}_2 \quad (54)$$

$$f_4 = -\frac{5}{8}\tilde{g}_0 - \frac{9}{16}\tilde{g}_2 \quad (55)$$

$$f_6 = \frac{1}{32}\tilde{g}_2 \quad (56)$$

On the other hand, for $m = 2$, this component takes the form

$$\begin{aligned} \hat{K}_{\eta\phi}(m = 2) = & f'_0 + f'_1 \cos(2\phi) + f'_2 \cos(2\phi - 6\theta) + f'_3 \cos(2\phi - 4\theta) + f'_4 \cos(2\phi - 2\theta) + \\ & f'_4 \cos(2\phi + 2\theta) - f'_3 \cos(2\phi + 4\theta) + f'_2 \cos(2\phi + 6\theta) \end{aligned} \quad (57)$$

where

$$f'_0 = \frac{3}{2}J \quad (58)$$

$$f'_1 = \frac{1}{8}\tilde{g}_0 \frac{1}{16}\tilde{g}_2 - \frac{3}{2}J \quad (59)$$

$$f'_2 = \frac{7}{64}\tilde{g}_2 \quad (60)$$

$$f'_3 = \frac{5}{16}\tilde{g}_0 - \frac{9}{32}\tilde{g}_2 \quad (61)$$

$$f'_4 = \frac{1}{4}\tilde{g}_0 - \frac{9}{64}\tilde{g}_2 \quad (62)$$

If we compare the constant components of Eq. (52) and Eq. (57), we see that f_0 incorporates both the total angular momentum J and the amplitude Q_0 , whereas f'_0 incorporates only J . Because of this, for low spin, the ADM mass increases more rapidly with amplitude for the axisymmetric cases, as can be seen in Fig. 4. As J increases, we see the effect of the Brill wave amplitude decreasing and approaching the pure Bowen-York values.

Fig. 5 shows J/M^2 as a function of the total angular momentum J for various values of the Brill wave amplitude Q_0 . Whereas the ADM mass increases more rapidly with amplitude for the axisymmetric cases, J/M^2 increases more rapidly for non-axisymmetric cases. Also, as J increases, we see the effect of the Brill wave amplitude decreasing and approaching the pure Bowen-York values. This is consistent with the above ADM mass results. Notice that for the Bowen-York data, J/M^2 does not converge to unity as discussed in [34]. This indicates that even for non-axisymmetric cases, J/M^2 for our initial data will never reach unity. However, it is interesting to point out that if we add a non-axisymmetric perturbation to the second fundamental form in [34], it would cause J/M^2 to increase even more.

B. Analysis of apparent horizons

In this Section we discuss the location and properties of the apparent horizon (AH) in these initial data sets. Studying the apparent horizon gives us a detailed understanding of the shape and mass of the black holes.

Defining s^μ to be the outward-pointing space-like unit normal of a two-sphere \mathcal{S} embedded in a constant time slice Σ with timelike unit normal n^μ , we can construct the outgoing null normal to any point on \mathcal{S} as $k^\mu = n^\mu + s^\mu$. The surface \mathcal{S} is called a marginally trapped surface if the divergence of the outgoing null vectors $\nabla_\mu k^\mu$ vanishes, or equivalently, if [35]

$$\Theta = D_i s^i + K_{ij} s^i s^j - K = 0, \quad (63)$$

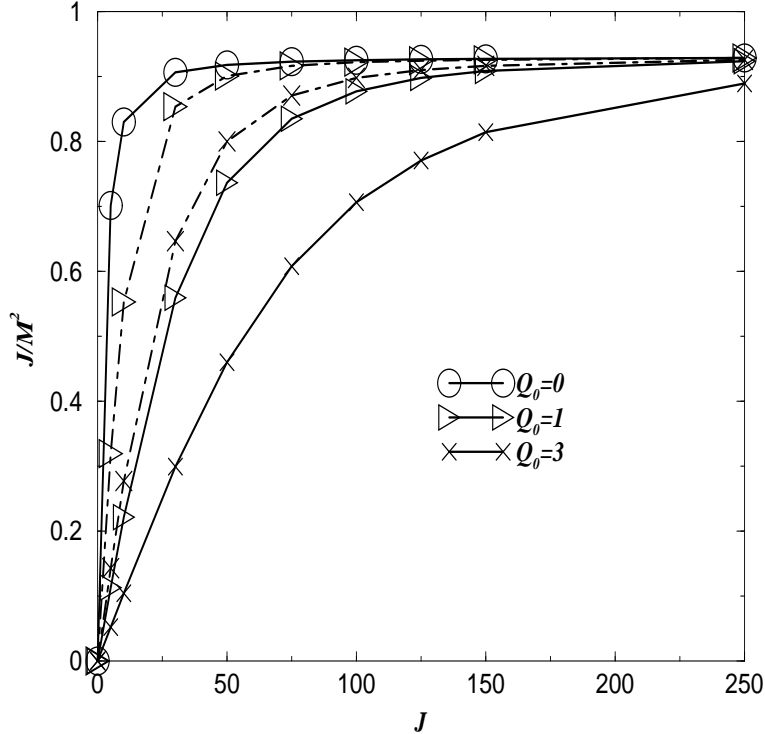


FIG. 5. We show J/M^2 as a function of the total angular momentum J for various values of the Brill wave amplitude Q_0 . The solid lines show the axisymmetric cases ($m = 0$), and the dashed line shows the non-axisymmetric cases ($m = 2$).

where Θ is the expansion of outgoing rays. The AH is defined as the outer-most marginally trapped surface.

By construction, all of our data sets contain an apparent horizon. Gibbons showed that an isometry surface, such as the throat, is an extremal area surface [36]. This means that in the some cases (for example, the time symmetric cases) the throat will be an apparent horizon. But, in general, the apparent horizon will not be on the throat.

We have computed the coordinate location of the apparent horizon in our initial data sets using the flow algorithm described in [37].

Fig. 6 shows the coordinate location of the apparent horizon for several non-rotating initial data sets. The parameters are $(Q_0, c) = (Q_0, 1)$ with the following values of Q_0 from the outer to the inner: $Q_0 = (-0.6, -0.5, -0.25, 0.25, 0.5)$. We observe that data sets with $Q_0 = (-0.25, 0.25, 0.5)$ have AH's which are on the throat, while data sets with $Q_0 = (-0.6, -0.5)$ form new horizons. Although the above results are only for a few examples, we observe that the azimuthal factor is large enough that the effective amplitude increase results in another minimal surface forming.

Fig. 7 shows the coordinate location of the apparent horizon for the axisymmetric rotating cases with parameters $(Q_0, J) = (1, J)$. The solid (outermost) line corresponds to $J = 0$. When J is increased, the AH tends to shrink. For high spin cases, the horizon will shrink. This behavior is similar to the location of the AH of Kerr. Thus, the AH's should be on the throat for the above parameter sets.

Fig. 8 shows the coordinate location of the apparent horizon for non-axisymmetric rotat-

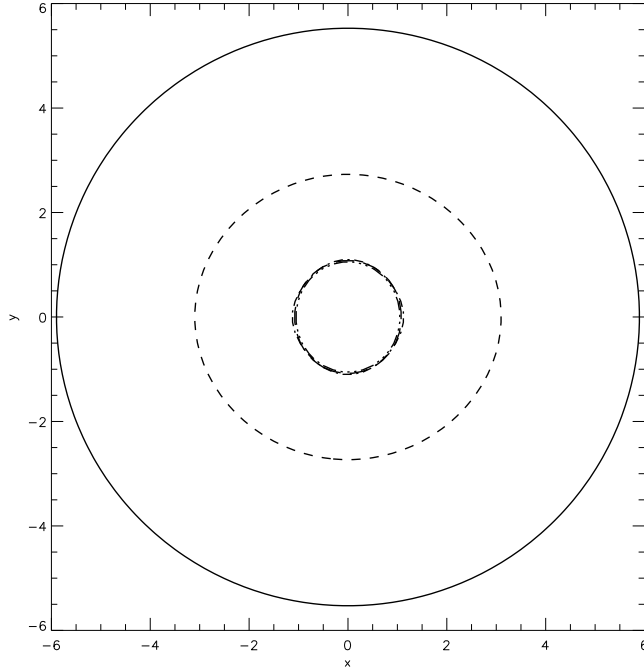


FIG. 6. The coordinate location of the apparent horizon is plotted for amplitudes $Q_0 = (-0.6, -0.5, -0.25, 0.25, 0.5)$. The other parameters are $(\eta_0, \sigma, c) = (0, 1, 1)$. The outermost AH corresponds to $Q_0 = -0.6$, and the dashed line corresponds to $Q_0 = -0.5$. The remaining data sets have an AH at the inner circle, which is the throat. Grid size (resolution) is $131^3(0.2)$.

ing cases with parameters the same as in the axisymmetric case: $(Q_0, J) = (1, J)$. The dot and dashed line (outermost) corresponds to $J = 75$ ($J/M^2 = 0.9$). For the rapidly spinning cases, horizons are expected to expand. This means that compared with axisymmetric cases, when we increase the Brill wave amplitude, the AH horizons will leave the throat easily.

When the apparent horizon is on the throat, it is a coordinate sphere. It is interesting, however, to study how distorted it is in the physical space. One measure of this distortion is the ratio of the polar to equator circumference: $C_r = C_P/C_E$. The polar circumference, C_P , is the proper length of the circumference which goes through the poles along a line of constant ϕ , and the equatorial circumference, C_E , is the proper length of equator, defined as $\theta = \pi/2$. In axisymmetry, this ratio is independent of ϕ , and is a single number which characterizes a data set once one has established the above definitions. In this case, if $C_P/C_E = 1$, the horizon is spherical, if $C_P/C_E < 1$ it is oblate, and if $C_P/C_E > 1$ it is prolate. In 3D, one can establish analogous definitions, although in this case C_P , and therefore C_r , is a function of ϕ .

Fig. 9 shows the ratio C_P/C_E for two values of ϕ for non-rotating cases with parameters $(Q_0, \eta_0, \sigma, c) = (Q_0, 0, 1, c)$. C_{P1} is the value of C_P at $\phi = 0$, and C_{P2} is the value of C_P at $\phi = \pi/2$. We observe that highly distorted features appear when $c > 0$ and $Q_0 > 0$.

For distorted rotating black holes, we study the same parameter sets as above: $(Q_0, \eta_0, \sigma, J, m) = (1, 0, 1, J, m)$. Fig. 10 shows C_r as a function of J for $m = 0$ and $m = 2$. Although the distortion patterns are different for axisymmetric and non-axisymmetric cases,

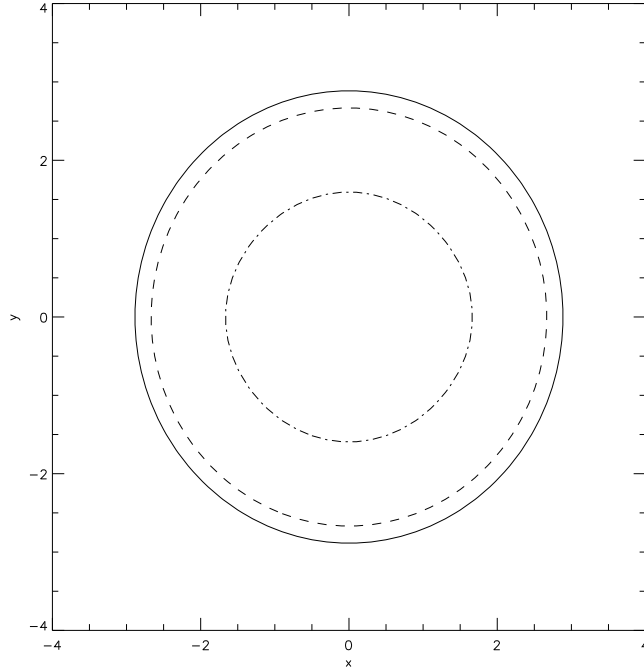


FIG. 7. The coordinate location of the apparent horizon of axisymmetric cases for various total angular momentum parameter J : 150, 30, and 0 which correspond J/M^2 : 0.9, 0.5, and 0 respectively. The solid line (outermost) is $J = 0$. When J is increased, the horizon shrinks.

both cases are nearly spherical for the range of parameters studied. High spin axisymmetric cases are slightly more oblate than the other cases. Also, for the non-axisymmetric cases, C_{P1} and C_{P2} are indistinguishable.

C. Maximum Radiation Loss (MRL)

Another quantity of interest which is related to the apparent horizon is the maximum radiation loss (MRL). The second law of black hole thermodynamics states that the area of the event horizon of a black hole, A_{EH} , cannot decrease in time. One can define a quantity associated with the area of black hole known as the irreducible mass, M_{irr} [38,39],

$$M_{irr} = \sqrt{\frac{A_{EH}}{16\pi}}. \quad (64)$$

By analogy to this quantity, one can define the mass of the apparent horizon given its area, A_{AH} ,

$$M_{AH} = \sqrt{\frac{A_{AH}}{16\pi}}. \quad (65)$$

More generally, for a rotating black hole, one can define the apparent horizon mass as

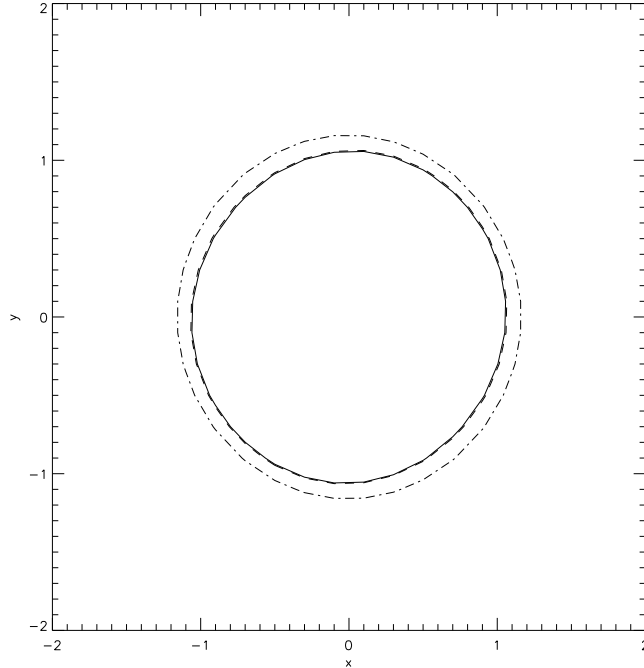


FIG. 8. The coordinate location of the apparent horizon of non-axisymmetric cases for various total momentum parameter J : 75, 10, and 0 which correspond J/M^2 : 0.9, 0.5, and 0 respectively. Contradictory to axisymmetry cases, the outermost one is high spin: $J = 75$.

$$M_{AH}^2 = \frac{A_{AH}}{16\pi} + \frac{4\pi J^2}{A_{AH}}, \quad (66)$$

where J is the total angular momentum.

One defines the radiation efficiency RE as the difference between the ADM mass of a spacetime and its irreducible mass in its final state:

$$RE = \frac{M - M_{irr,f}}{M}. \quad (67)$$

However, by second law of black hole thermodynamics, the final irreducible mass must be greater than or equal to the initial irreducible mass. Thus,

$$RE \leq \frac{M - M_{irr,i}}{M}. \quad (68)$$

Because one needs to perform an evolution to find the location of the event horizon on any slice, we can not compute the above fraction, even though it is for quantities defined on our data set. However, for our initial data sets, we know that the apparent horizon is the outer-most minimal area surface. It can be shown that if an apparent horizon exists, it must lie inside or coincident with an event horizon [40]. Thus the area of the event horizon on our initial slice must be greater than or equal to the area of the apparent horizon. Then we can define a quantity we call the maximum radiation loss (MRL) by using the ADM mass M :

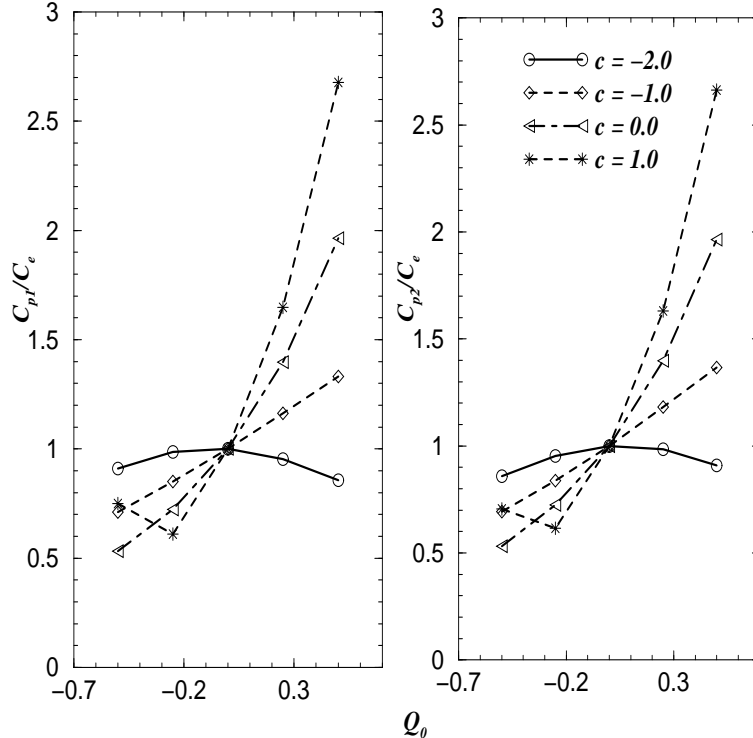


FIG. 9. The ratio C_P/C_E of non-rotating case for the parameter sets $(Q_0, \eta_0, \sigma, c) = (Q_0, 0, 1, c)$. C_{P1} is the value of C_P at $\phi = 0$, and C_{P2} is the value of C_P at $\phi = \pi/2$.

$$MRL = \frac{M - M_{AH,i}}{M} \geq RE. \quad (69)$$

The fraction above is an upper bound on the radiation efficiency. Therefore, we know that during an actual evolution, the total energy radiated has to be less than this amount. This will be a guide to choosing interesting initial data sets for evolution in the future.

Fig. 11 shows the MRL for non-rotating cases as a function of Q_0 and c for the family of initial data sets $(Q_0, \eta_0, \sigma, c) = (Q_0, 0, 1, c)$. The largest MRL is about 10% of the total mass. The sets within this family with the largest MRL s are those with both positive Q_0 and c , indicating that these might be interesting data sets to evolve.

Fig. 12 shows the MRL for rotating cases as a function of J and Q_0 for the family of initial data sets $(Q_0, \eta_0, \sigma, J) = (Q_0, 0, 1, J)$. For the axisymmetric cases, when the initial amplitude is larger the MRL tends to decrease, while for non-axisymmetric cases the trend is reversed for most values of J . Also, for the axisymmetric cases, the MRL increases as J becomes larger, but for non-axisymmetric cases the MRL decreases. As we saw for the ADM masses, when J is increased, the MRL for both classes of initial data approaches the pure Bowen and York values.

Furthermore, we can address an important question. Penrose proposed a criterion for a spacetime which, if violated, would indicate that Cosmic Censorship would be violated [41]. The criterion, the so-called Penrose inequality, is simply that the irreducible apparent horizon mass must be less than or equal to the ADM mass. This would result in a negative value of the MRL . Using the Brill wave plus black hole initial data, violations of the Penrose inequality were looked for in Ref. [1,2,42], but none were found. No violations were observed

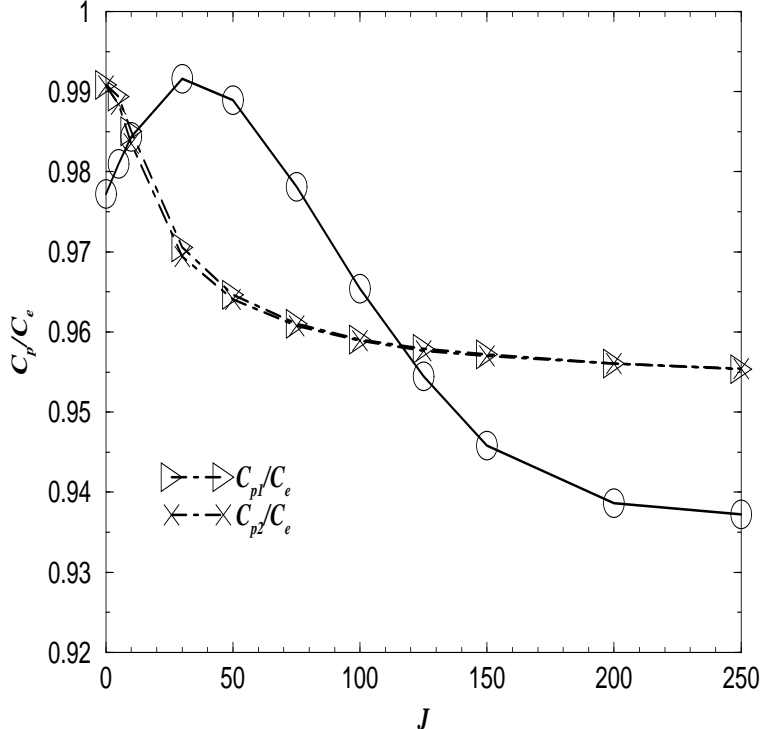


FIG. 10. The ratio C_P/C_E for axi- and non-axisymmetric rotating cases. The parameter sets are $(Q_0, \eta_0, \sigma, J) = (1, 0, 1, J)$. For non-axisymmetric cases, we have C_{P1} which is the value of C_P at $\phi = 0$, and C_{P2} which is the value of C_P at $\phi = \pi/2$. The solid line shows the axisymmetric case, and dashed lines show non-axisymmetric cases. High spin axisymmetric cases are slightly more oblate than the other cases.

in either our non-rotating or rotating initial data sets.

IV. CONCLUSIONS

We have extended Bernsteins's axisymmetric, distorted black hole data sets to full 3D by giving them a particular azimuthal dependence in the Brill wave function q . For rotating initial data, we have generalized axisymmetric distorted rotating black hole by allowing the conformal extrinsic curvature to have an azimuthal dependence.

From their physical properties, such as their ADM mass distortion of horizons and MRL , non-rotating axisymmetric cases are consistent with what has been observed by Bernstein's. In particular, Bernstein's results are recovered when the azimuthal parameter c is set to zero. However, rotating data sets are, by construction, different from those of Brandt and Seidel. For those initial data sets, we have seen that one of distortion parameters, Q_0 , strongly effects the physical properties when J is low, as we showed in Section III. However, as J is increased, physical properties are approaching the pure Bowen-York data. For further investigation of higher amplitude and spin cases for full 3D initial data as in Ref. [34], since we are using uni-grid Cartesian coordinate for all physical quantities except for the ADM mass, we need larger grid size and higher resolutions by using such as adaptive mesh refinement.

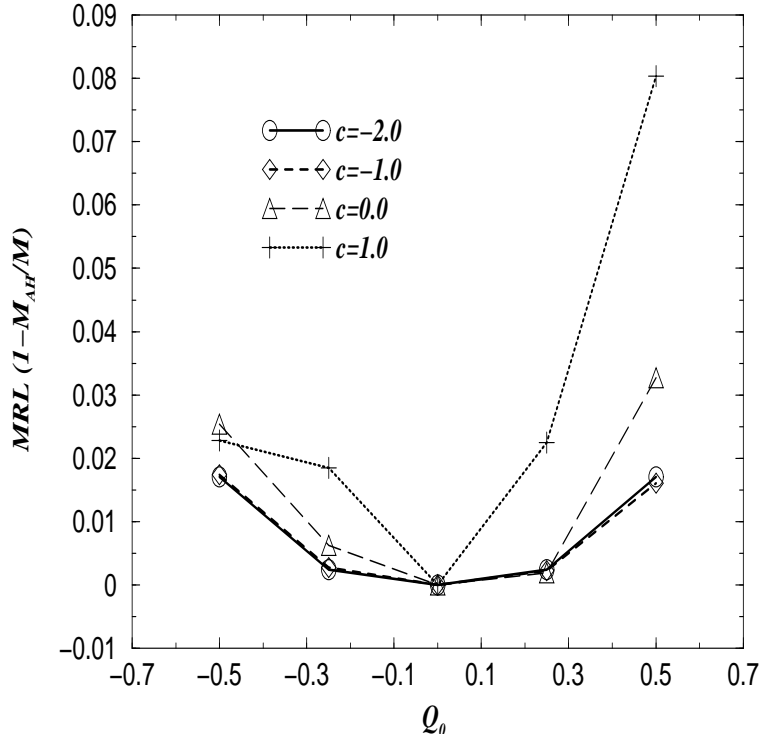


FIG. 11. We show the MRL for the initial data set: $(Q_0, \eta_0, \sigma, c) = (Q_0, 0, 1, c)$. The efficient $MRLs$ are for the positive amplitude and azimuthal factor.

In future papers we would like to address the radiation of angular momentum by evolving non-axisymmetric, distorted, rapidly-rotating black holes. Direct comparisons of radiative energy were done for axisymmetric and non-rotating initial data [20,21,22,43]. The close limit approximation studies are addressing radiated angular momentum [44,45]. However, as mentioned in Ref. [15], a direct comparison with full numerical simulations is under investigation. By using the Lazarus method [46,47], Ref. [15], one shows that initial data for grazing collisions cannot be mapped into the perturbative method. Although our non-axisymmetric, distorted rapidly rotating black holes are not necessarily astrophysically relevant, such analysis will provide an example of the usefulness of perturbation theory as an interpretive tool for understanding the dynamics produced in full nonlinear evolutions.

ACKNOWLEDGMENTS

We would like to thank our colleagues at AEI, Penn State, and TAC, Miguel Alcubierre, John Baker, Bernd Brügmann, Manuela Campanelli, Carlos O. Lusto, and Igor D Novikov. Special thanks to Sergio Dain for various discussion and comments. K. C. acknowledges support from Microsoft. Calculations were performed at the AEI on an SGI Origin 2000 and the Leibniz-Rechenzentrum on SR8000-F supercomputers.

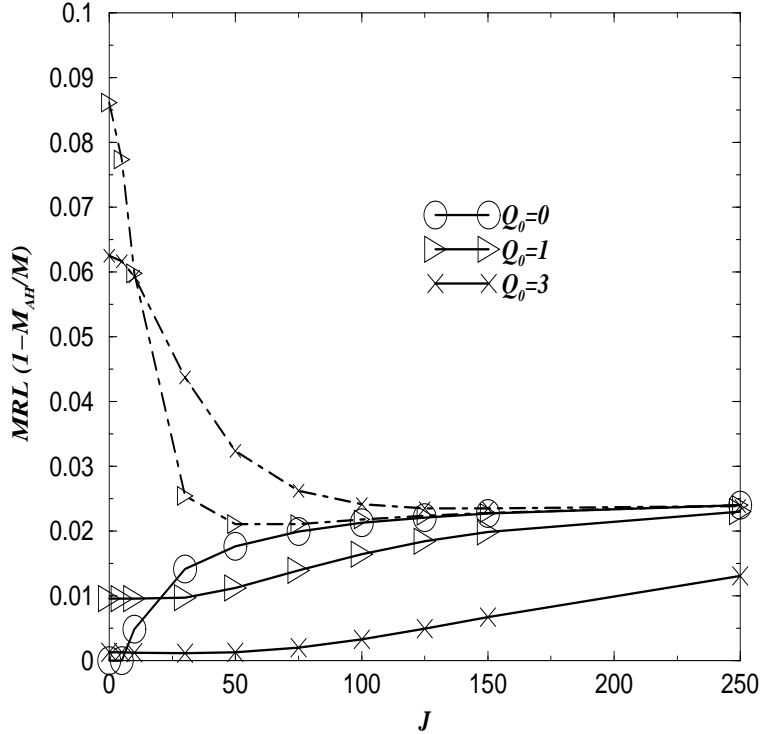


FIG. 12. We show the MRL for rotating cases. The initial data sets are $(Q_0, \eta_0, \sigma, J) = (Q_0, 0, 1, J)$. The solid lines show the axisymmetry cases, and the dashed line shows the non-axisymmetry cases.

REFERENCES

- [1] D. Bernstein, Ph.D. thesis, University of Illinois Urbana-Champaign, 1993.
- [2] S. Brandt and E. Seidel, Phys. Rev. D **54**, 1403 (1996).
- [3] A. A. Abramovici *et al.*, Science **256**, 325 (1992).
- [4] J. Hough, (1994), prepared for Edoardo Amaldi Meeting on Gravitational Wave Experiments, Rome, Italy, 14-17 Jun 1994.
- [5] Éanna É. Flanagan and S. A. Hughes, Phys. Rev. D **57**, 4535 (1998).
- [6] T. Damour, P. Jaranowski, and G. Schäfer, Phys. Lett. **B513**, 147 (2001).
- [7] T. Damour, P. Jaranowski, and G. Schäfer, Phys. Rev. **D63**, 044021 (2001).
- [8] T. Damour, P. Jaranowski, and G. Schäfer, Phys. Rev. **D62**, 084011 (2000).
- [9] P. Jaranowski and G. Schäfer, Phys. Rev. D **57**, 7274 (1998).
- [10] L. Blanchet *et al.*, Phys. Rev. Lett. **74**, 3515 (1995).
- [11] R. H. Price and J. Pullin, Phys. Rev. Lett. **72**, 3297 (1994).
- [12] W. Tichy, B. Brügmann, M. Campanelli, and P. Diener, (2002), gr-qc/0207011.
- [13] P. Anninos *et al.*, Phys. Rev. Lett. **71**, 2851 (1993).
- [14] S. Brandt *et al.*, Phys. Rev. Lett. **85**, 5496 (2000).
- [15] M. Alcubierre *et al.*, Phys. Rev. Lett. **87**, 271103 (2001), gr-qc/0012079.
- [16] A. Abrahams *et al.*, Phys. Rev. D **45**, 3544 (1992).
- [17] S. Brandt and E. Seidel, Phys. Rev. D **52**, 870 (1995).
- [18] M. Alcubierre *et al.*, Phys. Rev. D **64**, R61501 (2001).

- [19] S. Brandt, K. Camarda, and E. Seidel, in *Proceedings of the 8th Marcel Grossmann Meeting on General Relativity*, edited by T. Piran (World Scientific, Singapore, 1999), pp. 741–743.
- [20] G. Allen, K. Camarda, and E. Seidel, (1998), gr-qc/9806014, submitted to Phys. Rev. D.
- [21] G. Allen, K. Camarda, and E. Seidel, (1998), gr-qc/9806036, submitted to Phys. Rev. D.
- [22] J. Baker *et al.*, Phys. Rev. D **62**, 127701 (2000), gr-qc/9911017.
- [23] M. Alcubierre *et al.*, (2001), in preparation.
- [24] K. Camarda, Ph.D. thesis, University of Illinois at Urbana-Champaign, Urbana, Illinois, 1998.
- [25] J. York, in *Sources of Gravitational Radiation*, edited by L. Smarr (Cambridge University Press, Cambridge, England, 1979).
- [26] D. S. Brill, Ann. Phys. **7**, 466 (1959).
- [27] M. Bondarescu, M. Alcubierre, and E. Seidel, Class.Quant.Grav. **19**, 375 (2002).
- [28] S. Brandt and E. Seidel, Phys. Rev. D **52**, 856 (1995).
- [29] J. Bowen and J. W. York, Phys. Rev. D **21**, 2047 (1980).
- [30] S. Dain, (2002), gr-qc/0207090.
- [31] S. Dain and H. Friedrich, Comm. Math. Phys. **222**, 569 (2001).
- [32] R. Arnowitt, S. Deser, and C. W. Misner, in *Gravitation: An Introduction to Current Research*, edited by L. Witten (John Wiley, New York, 1962), pp. 227–265.
- [33] N. O’Murchadha and J. York, Phys. Rev. D **10**, 2345 (1974).
- [34] S. Dain, C. O. Lousto, and R. Takahashi, Phys. Rev. D **65**, 104038 (2002).
- [35] J. York, in *Frontiers in Numerical Relativity*, edited by C. Evans, L. Finn, and D. Hobill (Cambridge University Press, Cambridge, England, 1989), pp. 89–109.
- [36] G. Gibbons, Commun. Math. Phys. **27**, 87 (1972).
- [37] M. Alcubierre *et al.*, Class. Quantum Grav. **17**, 2159 (2000).
- [38] D. Christodoulou, Phys. Rev. Lett. **25**, 1596 (1970).
- [39] G. Cook, Ph.D. thesis, University of North Carolina at Chapel Hill, Chapel Hill, North Carolina, 1990.
- [40] S. W. Hawking, in *Black Holes*, edited by C. DeWitt and B. S. DeWitt (Gordon and Breach, New York, 1973), pp. 1–55.
- [41] R. Penrose, Ann. N.Y. Acad. Sci. **224**, 125 (1973).
- [42] D. Bernstein, D. Hobill, E. Seidel, and L. Smarr, Phys. Rev. D **50**, 3760 (1994).
- [43] J. Baker *et al.*, Phys. Rev. D **55**, 829 (1997).
- [44] G. Khanna *et al.*, Phys. Rev. Lett. **83**, 3581 (1999).
- [45] G. Khanna, R. Gleiser, R. Price, and J. Pullin, New Jour. Phys. **2**, 3 (2000).
- [46] J. Baker, B. Brügmann, M. Campanelli, and C. O. Lousto, Class. Quantum Grav. **17**, L149 (2000).
- [47] J. Baker, M. Campanelli, and C. O. Lousto, Phys. Rev. **D65**, 044001 (2002).